González Suárez, A.; Gutierrez-Herrera, E.; Berjano, E.; Jimenez Lozano, JN.; Franco, W. (2015). Thermal and elastic response of subcutaneous tissue with different fibrous septa architectures to RF heating: numerical study. Lasers in Surgery and Medicine. 47(2):183-195. doi:10.1002/lsm.22301.

Thermal and elastic response of subcutaneous tissue with different fibrous septa architectures to RF heating: numerical study

Ana González-Suárez, PhD[1, #], Enoch Gutierrez-Herrera, PhD[2, ##], Enrique Berjano, PhD[1], Joel N. Jimenez Lozano, PhD[2, ###], Walfre Franco, PhD[2*]

[1] Biomedical Synergy, Electronic Engineering Department, Universitat Politècnica de València, Valencia, 46022, Spain

[2] Wellman Center for Photomedicine, Massachusetts General Hospital, Department of Dermatology, Harvard Medical School, Boston, Massachusetts, 02114, USA

[#]Visiting Graduate Student at Wellman Center for Photomedicine

[##]Current affiliation: Centro de Ciencias Aplicadas y Desarrollo Tecnólogico, Universidad Nacional Autónoma de México, México DF, México

[###]Current affiliation: Zeltiq Aesthetics Inc, Pleasanton, CA 94588, USA

[*]Correspondence to: Walfre Franco, PhD, Wellman Center for Photomedicine, 50 Blossom St, Boston, MA 02114. Email: wfranco@mgh.harvard.edu

Conflict of interest Disclosures: All authors have completed and submitted the ICMJE Form for Disclosure of Potential Conflicts of Interest and none were reported.

Background: Radiofrequency currents are commonly used in dermatology to treat cutaneous and subcutaneous tissues by heating. The subcutaneous morphology of tissue consists of a fine, collagenous and fibrous septa network enveloping clusters of adipocyte cells. The architecture of this network, namely density and orientation of septa, varies among patients and, furthermore, it correlates with cellulite grading.

Objectives: In this work we study the effect of two clinically relevant fibrous septa architectures on the thermal and elastic response of subcutaneous tissue to the same RF treatment; in particular, we evaluate the thermal damage and thermal stress induced to an intermediate- and a high-density fibrous septa network architecture that correspond to clinical morphologies of 2.5 and 0 cellulite grading, respectively.

Materials and Methods: We used the finite element method to assess the electric, thermal and elastic response of a two-dimensional model of skin, subcutaneous tissue and muscle subjected to a relatively long, constant, low-power RF treatment. The subcutaneous tissue is constituted by an interconnected architecture of fibrous septa and fat lobules obtained by processing micro-MRI sagittal images of hypodermis. As comparison criteria for the RF treatment of the two septa architectures, we calculated the accumulated thermal damage that corresponds to 63% loss in cell viability.

Results: Electric currents preferentially circulated through the fibrous septa in the subcutaneous tissue. However, the intensity of the electric field was higher within the fat because it is a poor electric conductor. The power absorption in the fibrous septa relative to that in the fat varied with septum orientation: it was higher in septa with vertical orientation and lower in septa with horizontal orientation. Overall, maximum values of electric field intensity, power absorption and temperature were similar for both fibrous septa architectures. However, the high-density septa

architecture (cellulite grade 0) had a more uniform and broader spatial distribution of power absorption, resulting in a larger cross-sectional area of thermal damage (≈1.5 times more). Volumetric strains (expansion and contraction) were small and similar for both network architectures. During the first seconds of RF exposure, the fibrous septa were subjected to thermal expansion regardless of orientation. In the long term, the fibrous septa contracted due to the thermal expansion of fat. Skin and muscle were subjected to significantly higher Von Mises stresses (measure of yield) or distortion energy than the subcutaneous tissue.

Conclusions: The distribution of electric currents within subcutaneous tissues depends on tissue morphology. The electric field is more intense in septum oriented along the skin to muscle (top to bottom) direction, creating lines or planes of preferential heating. It follows that the more septum available for preferential heating, the larger the extent of volumetric RF-heating and thermal damage to the subcutaneous tissue. Thermal load alone, imposed by long-exposure to heating up to 50 ºC, results in small volumetric expansion and contraction in the subcutaneous tissue. The subcutaneous tissue is significantly less prone to non-reversible deformation by a thermal load than the skin and muscle.

Keywords: cellulite, fat, fibrous septa, hyperthermia, hypodermis, modeling, radiofrequency heating, skin, tissue mechanics

INTRODUCTION

Radiofrequency (RF) medical devices are commonly used to heat up tissues to specific target temperatures that vary for different procedures, ranging from a few degrees for low hyperthermia applications to more than 100 ºC for tissue ablation applications. RF devices circulate electric currents oscillating at radio frequencies (MHz) through tissue. Electric currents enter the tissue at the source tip or active electrode and exit at the return, which is either a second active electrode (bipolar RF) or a distant dispersive pad (monopolar RF). In many clinical applications, the underlying physics of the thermal response of tissue to RF heating are relatively straightforward because the electrode is in contact with the target tissue and the target tissue is homogenous (one type of tissue); that is, the electric and thermal environments within the tissue are continuous. In non-invasive cutaneous and subcutaneous clinical applications electric currents travel through different tissues that are far from homogenous, such as the subcutaneous tissue, resulting in more complex physical interactions between electric currents and tissues. Applications in dermatology include skin tightening, reduction of wrinkles, and treatments for acne and cellulite [1, 2]. For example, RF-heating is commonly used to cause the shrinkage of dermal collagen and induce stimulation of fibroblast cells that produce new collagen [3]. More recently, it has been used to denaturate adipocyte cells and to reduce the thickness of the subcutaneous tissue layer [4].

The subcutaneous morphology of tissue consists of a fine, collagenous and fibrous septa network enveloping clusters of adipocyte cells. The fat, enclosed within adipocytes, and septa present different electric environments to the current flowing through, as well as different thermal environments to the heat generated by the current flow [5]. Furthermore, the density and orientation of the fibrous septa network varies significantly from person to person, and it is well known that these variations in network architecture correlate to different cellulite grades. Herein,

the term density makes reference to the space occupied by the fibrous septa network; the more space-filling the network is, the higher the density. Cellulite grades are assessed by visual inspection according to skin appearance and scaled from Grade 0, smooth skin, to Grade 4 “cottage cheese” appearance. The grade correlates with the percentile of adipose tissue versus connective tissue in a given volume of hypodermis and invaginations inside the dermis [6].

Despite the electrical, thermal and structural complexity of the subcutaneous tissue, it is commonly regarded as a uniform layer of fat [7] and the circulation of currents as a one-dimensional linear electric flow [2]; that is, heating is considered proportional to the resistivity of tissue. Furthermore, it is also commonly assumed that the distribution of electric currents depends solely on the geometry of the electrode [8]. However, in a recent study, it was shown that by altering the direction of the RF-induced internal electric field the heat deposition within the fat could be selective and precisely localized [9]. This study highlighted the multi-dimensional non-linear nature of the electric current and tissue interactions. A later study found that the septa favors the flux of electric current and heat dissipation, which varies with the relative orientation of septa to the direction of the electric field [5]. This later study showed that the structural configuration of septa affects the electric field distribution and, hence, heat deposition within the subcutaneous tissue. In addition, this work suggested that the distribution of thermal stresses within the subcutaneous tissue is non-uniform, with the septa and fat most likely subjected to different stress intensities. Since the structural configuration of septa affects the electric field, it is likely that the same RF exposure for different configurations of septa would result in different thermal responses. A clinical output common to RF treatments is change in volume and shape of cutaneous and subcutaneous tissues. Changes in tissue volume and shape induced by heating are due to several related process, such as, cell injury and death,

collagen denaturation, tissue expansion and contraction. The contribution of each process to deformation of tissue is not known. The influence of subcutaneous tissue morphology on RF heating, however important to RF treatments, is not known either.

OBJECTIVES

[[The objective of the present work is to study the effect of two clinically relevant fibrous septa architectures on the thermal and elastic response of subcutaneous tissue to RF heating. In particular, we evaluate the thermal damage and thermal stress induced to an intermediate- and a high-density fibrous septa network architecture by the same RF treatment. These architectures correspond to cellulite grading of 2.5 and 0, respectively.]]

MATERIALS AND METHODS

We used the finite element method to simulate the electric, thermal and elastic response of a two-dimensional model of skin, subcutaneous tissue and muscle subjected to a relatively long, constant, low-power RF exposure. The interconnected architecture of fibrous septa and fat lobules was obtained by processing micro-MRI sagittal images of hypodermis. As comparison criteria for the RF treatment output, we calculated the extent of accumulated thermal damage that corresponds to 63% loss in cell viability.

Model Geometry

The model geometry and dimensions are shown in Figure 1. [[The central geometry beneath the RF applicator was mirrored laterally (both sides) to extend the domain thereby eliminating numerical boundary artifacts in the solution. The geometry in Figure 1 corresponds to high-

density fibrous septa and was obtained as described in [5]. The RF applicator is actively cooled and does not exert pressure on the skin, it was modeled as an adhesive-type electrode with a boundary condition. A more in detail description of model geometry is included in the Appendix.]]

Governing Equations

The electric response of tissue to RF currents was modeled with the Laplace's equation. The thermal and elastic responses to RF heating were modeled with the bioheat equation, including an additional thermo-elastic term, and the equation of motion for an isotropic linear elastic solid.

Electric Propagation

Electric propagation is assumed time independent since it is very fast compared to heat diffusion and the thermo-elastic response. We use a quasi-static formulation to model the response of tissue to electric fields. In the quasi-static approximation the characteristic length of the object of study is much less than the wavelength of the electromagnetic field: herein, the thickness of skin and fat is ~0.003 meters and the wavelength of the incident electromagnetic wave at 1 MHz is 300 meters. A quasi-static approach means that the spatial distribution of the electromagnetic fields over the extent of the device is the same as that of static fields [10]. Since biological tissue can be considered almost totally resistive, most of the electrical power is deposited in a small zone close to the electrode.

In biological tissue the rate of energy dissipated per unit volume at a given point is directly proportional to the electric conductivity of the tissue κ (S/m) and to the square of the induced internal electric field **E** (V/m), that is,

$$Q_i = \kappa_i |\mathbf{E}_i|^2/2, \quad (1)$$

where Q is the power absorption (W/m^3) and $|\mathbf{E}|$ is the norm of the vector electric field. $\mathbf{E}$ is calculated from $\mathbf{E}_i = -\nabla V_i$, where V is the voltage (V) obtained by solving the Laplace's equation

$$\nabla \cdot (\kappa_i \nabla V_i) = 0, \quad (2)$$

where the subscript denotes skin, fibrous septa (connective tissue), fat or muscle, i.e., i={s, c, f, m}.

Heat Diffusion

The bioheat transfer equation in tissue [11] including the additional thermo-elastic term can be written as

$$\rho_i c_i \frac{\partial T_i}{\partial t} + \rho_i c_i \boldsymbol{u}_i \cdot \nabla T_i = \nabla \cdot (k_i \nabla T_i) + Q_M + \rho_b c_b \omega_i (T_b - T_i) + Q_i, \quad (3)$$

where ρ is the density of the tissue in (kg/m^3), c is the specific heat of the tissue in (J/kg/K), t is the time in (s), $T(x,y,t)$ is the temperature in (K), $\boldsymbol{u}$ = {u,v} is the displacement vector in (m), k is the thermal conductivity in (W/m/K), Q_M is the metabolic heat generation in (W/m^3), ρ_b is the blood density in (kg/m^3), c_b is the blood specific heat in (J/kg/K) [13], ω is the blood perfusion rate in (kg/m^3/s), T_b is the arterial temperature in (K), and Q is the power absorption. Q_M was neglected because its contribution is significantly small relative to other terms [12].

Elastic Deformation

The motion equation for an isotropic linear elastic solid is used to describe movement and deformation of tissue,

$$\rho_i \frac{\partial^2 \boldsymbol{u}_i}{\partial t^2} - \nabla \cdot \boldsymbol{\sigma}_i = \boldsymbol{F}_v, \quad (4)$$

where $\boldsymbol{\sigma}$ is the stress tensor in (Pa) and $\boldsymbol{F}_v$ denotes the external volume forces in (Pa/m^2). Constitutive relations for an isotropic linear elastic material are the following: (i) the stress tensor $\boldsymbol{\sigma} = [\boldsymbol{S}(\boldsymbol{I} + \nabla \boldsymbol{u})]$, where $\boldsymbol{S}$ is the Duhamel term which relates the stress tensor to the strain tensor and temperature, $\nabla \boldsymbol{u}$ the displacement gradient and $\boldsymbol{I}$ the identity matrix; (ii) the Duhamel relation $\boldsymbol{S} - \boldsymbol{S}_0 = \boldsymbol{C} : (\in - \alpha(T - T_0) - \in_0)$, where $\boldsymbol{C}$ is the 4th order elasticity tensor, ":" denotes the double-dot tensor product (or double contraction), ϵ is the strain tensor, $\boldsymbol{S}_0$ and ϵ_0 are initial stresses and strains, α is the thermal expansion coefficient in (1/°C), and T_0 is the initial temperature; and (iii) the strain tensor written in terms of the displacement gradient, $\in = [\nabla \boldsymbol{u}^T + \nabla \boldsymbol{u}]/2$. The formulation of Eq. 4 is Lagrangian, that is, the frame of reference for the computed stress and deformation is the material initial configuration. When solid objects deform due to external or internal forces and constraints, each material particle keeps its coordinates $\boldsymbol{X}$, while spatial coordinates $\boldsymbol{x}$ change with time and applied forces such that they follow a path $\boldsymbol{x} = \boldsymbol{X} + \boldsymbol{u}(\boldsymbol{X}, t)$ in space. Since the material coordinates are constant, the current spatial position is uniquely determined by the displacement vector $\boldsymbol{u}$. Material properties are also derived in a material frame of reference in the coordinate system $\boldsymbol{X}$.

Tissue Properties

The electric, thermal and mechanical properties of skin, fat, fibrous septa and muscle are assumed constant and temperature independent [4, 14-17] (Table 1). Electrical properties are frequency dependent and those used herein correspond to 1 MHz [18]. However, the electric conductivity remains fairly constant for frequencies from 10^3 to 10^6 Hz and the permittivity decreases by one order of magnitude in the same frequency range [18]. Thus the electric response of tissue within this frequency range is qualitatively similar. Perfusion is also assumed

constant and negligible in the septa, $\omega_c = 0$. Within 38 to 45 ºC, variations in specific heat [19], thermal conductivity [20] and blood perfusion are not significant [7]. Electrical and thermal properties of fibrous septa bundles are assumed to be similar to those of the dermis since it is a collagenous tissue [5]. For tissue as an isotropic linear elastic material, strains and displacements are small and the elastic properties are independent of direction, hence, tissue can be characterized by the Young's modulus and Poisson's ratio.

Boundary and Initial Conditions

Table 2 shows the electrical, thermal and elastic boundary conditions applied to the governing Equations (2)-(4). The RF applicator atop the skin surface was modeled as a boundary condition of constant voltage distribution:

$$V_0(-L \le x \le L) = [a\left(\frac{lx}{L}\right)^2 + b]\sqrt{PZ}\,, \tag{5}$$

where P (150 W) is the applied RF power, Z (100 Ω) the total tissue impedance, and a ($-2.25 \cdot 10^{-3}$ and b (1.28) are correlation constants [4] for a monopolar applicator operating at 1 MHz. Zero voltage was applied to the bottom muscle boundary, simulating the electrical performance of a dispersive electrode. Null electrical current was applied to the remaining skin surface and lateral boundaries. At the skin surface beneath the RF applicator T_r = 30 ºC. For the remaining skin surface, a free convection condition was used to simulate cooling by room air: heat transfer coefficient $h_{a\text{-}s}$=10 W/m^{2}K and ambient temperature T_a=25 ºC. Zero thermal flux was applied to the lateral boundaries. Constant core body temperature T_c = 37 ºC was set at the muscle bottom. Regarding the elastic boundary conditions, a free movement condition was used at the lateral boundaries to simulate the absence of constraints and loads. A fixed constraint condition on the upper skin and lower muscle surfaces was applied to simulate zero displacement in the vertical

direction. [[Everywhere else continuity was used to satisfy internal boundary conditions, including boundaries between fibrous septa and fat.]] Initial conditions were zero voltage and strain and 37 ºC.

Thermal Damage

We used thermal damage as criteria of comparison between treatments for different fibrous septa architectures subjected to the same RF exposure. Thermal damage is assumed a first order kinetic process and calculated with the Arrhenius equation [21, 22], which relates cell viability to temperature and exposure time as

$$\Omega(\tau) = \ln\left\{\frac{C(0)}{C(\tau)}\right\} = \int_0^{\tau} A e^{\frac{-E_a}{RT(t)}} dt, \tag{6}$$

where $\Omega(\tau)$ is the logarithm of the ratio of initial concentration $C(0)$ to actual concentration $C(\tau)$, τ the total heating time in (s), R the universal gas constant, A the frequency factor in (1/s), and E_a the activation energy for an irreversible reaction in (J/mol). From experiments of skin heating within 44--50 ºC temperature range, $A = 2.2\times10^{124}$ s^{-1} and $\Delta E = 7.8\times10^{5}$ J/mol [23]. Contours of $\Omega = 1$ that represent 63% reduction in viability or the threshold for completely irreversible thermal damage were used to compare RF treatment outputs.

RESULTS

The electric, thermal and elastic response of two different fibrous septa architectures to the same RF exposure (150 W) is presented next. [[The governing equations were solved as described in the Appendix. The electric response is instantaneous and time-independent. The thermal and elastic responses correspond to 8000 s of exposure to 150 W of RF power. The

length of the exposure was chosen to reach steady states in temperature and elastic deformation.]]

Electric Propagation

Voltage distributions and depth profiles are shown in Figure 3. Voltage distributions and intensities appear similar between intermediate and high-density septa architectures. However, a less symmetric voltage distribution sensitive to the position of the electrode, relative to the septa, developed in the intermediate-density septa architecture, Figure 3a. The high-density fibrous septa has a more symmetric voltage distribution independent of electrode position, Figure 3b. Voltage profiles also appear similar between fat and septa architectures as illustrated by the depth profile at $x = 0$, Figure 3c. Electric field distributions and depth profiles are shown in Figure 4. Distributions and intensities of the electric field visibly vary between architectures and between fat and septa. For the high-density architecture the overall maximum value of the electric field is 4.321 V/mm, for the intermediate-density architecture is 3.365 V/mm. Along the depth profile at $x = 0$ the strength of the electrical field in the fat is clearly greater than in the septa: the line profiles in Figures 4c and d show abrupt increments where the electric field corresponds to fat, or conversely large drops in intensity at the fibrous septa. Distributions of electric power absorption and electric displacement within the tissue are shown in Figure 5. In skin, the electric field is much more intense by the edges of the RF applicator, resulting in higher power absorption in the skin beneath the edges relative to the rest of the skin. Overall, the highest power absorption is in the fibrous septa that favor the flow of electric currents (zoom area, Figure 5).

Heat Diffusion and Thermal Damage

Temperature distributions after long exposures to RF heating are shown in Figure 6. The heating was mainly confined to the subcutaneous tissue because of surface cooling, higher subcutaneous power absorption and slow subcutaneous heat diffusion. The maximum temperature for the intermediate-density fibrous septa network is a little lower than that for the high-density network; T_{max} = 48.12 and 49.28 ºC, respectively. Temperature distributions are also similar. The evolution in time of temperature depth profiles at x = 0 are shown in Figure 7. Depth profiles followed similar dynamics: within the skin, the profile is linear, remained confined to lower temperatures and varied very little because of cooling; within the subcutaneous tissue, the profile is parabolic and the peak height and location increases and goes deeper as time progresses; within the muscle, the profile follows a non-linear decay to core temperature. Arbitrarily dividing the thickness of the subcutaneous fat layer ($l_{c,f}$ = 17 mm) in two (8.5 mm), larger differences in temperature occurred in time within the bottom region (10 < y < 18.5), where the high-density fibrous septa architecture reached higher temperatures. For both architectures, the thermal damage was mostly confined to the subcutaneous tissue while sparring the skin, Figure 6. For the high-density fibrous septa architecture, the cross-sectional extent of thermal damage was ≈ 1.5 times larger and reached a small area in the muscle, Figure 6(b).

Thermo-elastic Deformation

Volumetric strain quantifies deformation of tissue from its original volume. Distributions of volumetric strain at specific times (25 and 8000 s) are shown in Figure 8. Initially (t = 25 s) most of the subcutaneous tissue (fat lobules and fibrous septa) was subjected to expansion (positive volumetric strain), which was larger in the fibrous septa than in the fat. In steady state (t = 8000

s), expansion of the fat lobules continues because of an increased volumetric strain. However, the fibrous septa contracts as indicated by a negative volumetric strain. The skin is always subjected to contraction (negative and constant volumetric strain) because of contact with the cooling surface. The evolution of volumetric strain depth profiles at $x = 0$ are shown in Figure 9 for both fibrous septa architectures. Every profile shows a relative smooth curve with abrupt increments (t= 25 s) or drops (t= 1225 and 8000 s) in strain at the fibrous septa. These profiles show an increased expansion of fat lobules with depth until a peak is reached. The peak coincides with the region of high temperatures. In addition the profiles show the interplay between expansion of the fat lobules and shrinkage of the fibrous septa: the fibrous septa initially expand faster and more than the fat (t = 25 s), eventually the fat catches up squeezing the septa (t = 1225 s).

All materials have an associated yield strength, which is a measure of their elastic limit, and will not return to their original shape if the stress is removed. In an elastic body that is subject to loads in 3 dimensions, a complex system of stresses is developed: at any point within the body there are stresses acting in different directions, and the direction and magnitude of stresses change from point to point. The Von Mises criterion is a formula for calculating whether the stress combination at a given point will cause failure. Distributions of the Von Mises stress in response to the RF thermal load are shown in Figure 10. Von Mises stress distributions are relatively similar for both fibrous septa architectures at the skin and subcutaneous tissue layers. At the muscle, the Von Mises stress distribution for the high-density architecture shows a wider and deeper reach than that for the intermediate-density architecture. Von Mises stress in the skin was more uniform because of thermal contact with the cold surface. In the muscle it was higher close to the subcutaneous tissue region where the highest temperatures occurred. Overall, the

skin and muscle were subjected to a higher Von Mises stress or distortion energy than the subcutaneous tissue. The subcutaneous tissue is more elastic and, thus, able to withstand larger thermal loads without yield. The depth profile of the von Mises stress shows abrupt drops and rises at the skin-subcutaneous tissue and subcutaneous tissue-muscle interfaces, Figure 10c.

DISCUSSION

Electric power absorption is directly proportional to the electric conductivity of the tissue and the square of the intensity of the internal electric field, Eq. (1). The electric conductivity of fibrous septa is one order of magnitude larger than the conductivity of fat in subcutaneous tissues, Table 1, presenting a more favorable medium for circulation of electric currents. Since the tissue physical properties are constant, the power absorption at specific tissue locations is truly set by the internal electric field, which in turn is set by the morphology of tissue. Figure 4 illustrates the complexity in the distributions of the internal electric field that emerges from differences in electrical properties and variations in morphology. An additional variable not explicitly illustrated is the incidence of the electric field [9], for example, the electric field at the center of the electrode is perpendicular to the tissue interface while towards the edge the incidence is at an angle. Overall, the intensity of the electric field is larger in fat than in septum because the voltage drops more when current circulates through fat --- lower conductivity implies higher resistivity --- than when circulating through fibrous septum. By definition, the electric field is equal to the negative gradient of the electric potential. Regarding the fibrous septa on its own, the intensity of the electric field varies with the orientation and location of septum relative to the incident electric field and position of the electrode. Intensity is higher in septum perpendicularly oriented to the skin surface (vertical) and lower in septum parallel to the surface (horizontal). It is this

difference in orientation what sets the main heat sources in the subcutaneous tissue since the absolute largest absorption of electric power occurs in septum oriented from top to bottom, creating lines or planes (in 3D) of preferential heating as illustrated in Figure 5. Note that the power absorption in fat is higher than the power absorption in septum oriented horizontally.

Variations in the density of fibrous septa result in variations on the number of septum available for preferential heating. A high-density morphology, like the one corresponding to cellulite grade 0, has more lines or planes of high power absorption spaced relatively closer to each other; thus, larger volumes of subcutaneous tissue are subjected to RF heating and, subsequently, larger volumes of non-reversible thermal damage are created, Figure 6. The converse is true for intermediate and low-density morphologies, cellulite grades of 2.5 and 4, for which fewer septum oriented for preferential heating and spaced further apart result in smaller volumes of subcutaneous tissue damaged thermally. Note that regardless of fibrous septa density the heating is confined to the subcutaneous tissue and skin. In other words, the intensity of the electric field is significantly small in muscle and the power absorption is negligible there. A cooling surface bounds the temperature in the skin, but Figure 5 shows that the power absorption is dominant in the subcutaneous tissue septa and the skin by the edge of the RF electrode; that is, there is instantaneous generation of heat in the skin and subcutaneous tissue regardless of the cooling scheme or RF exposure.

In long-term RF heating exposures, the temperature of adjacent septa and fat is uniform because of the heat diffusion from septa into fat, or from fat into septa (depending on location). These uniform temperature fields result in uniform thermal loading, which is influenced by local temperatures and tissue properties rather than by fibrous septa density and orientation, as illustrated by distributions of the volumetric strain in Figure 8. The estimated initial expansions

and subsequent contractions of the fibrous septa are small, which may be an understatement since we are not accounting for collagen denaturation in modeling elasticity. It is well established that heat can cause shrinkage to connective tissues by disrupting the molecular bonding of collagen [24]. So considering the distributions of instantaneous power absorption, a high-power and short RF exposure would cause collagen denaturation in the skin (no cooling) beneath the electrode edges and the fibrous septa aligned for preferential heating. The rest of the skin and the fat would probably be spared from damage because of the much lower power absorption in these regions.

In summary, the morphology of the subcutaneous tissue gives rise to a complex distribution of the internal electric field established by RF currents. The density and orientation of the fibrous septa network yields the complexity in the electric response. Thermally, the subcutaneous tissue response is relatively simpler because of thermal equilibrium. However, the fibrous septa still matters. Figure 11 shows the non-reversible thermal damage response to a RF exposure assuming the subcutaneous tissue is constituted by fat only; the RF power (200 W) was adjusted to induce damage to the subcutaneous tissue --- as it is done in planning treatments. The figure also shows the non-reversible thermal damage response of the subcutaneous tissue including septa: the presence of septa resulted in subcutaneous zones of damage 2 to 3 times larger than with fat only. A larger treatment zone is not necessarily unfavorable. Although in these particular cases larger treatment zones resulted in damage to the muscle.

[[

Clinical Relevance

Results suggest that patients with cellulite Grade 0 would have a better response than patients with cellulite Grade 2.5 if both were subjected to the same RF treatment. As discussed,

this is because of the difference in architecture of the fibrous septa networks. Assuming that the treatment response is proportional to the volume of tissue with irreversible thermal damage (Fig. 6), then the RF treatment should be modified to improve the response of patients with more cellulite. Increasing the RF power would enlarge the response volume, it could damage muscle as well if the blood perfusion in muscle was not able to sink or remove excess heat. Alternatively the RF energy could be delivered in higher-power pulses that would gradually increase the temperature of the fat while the temperature in the skin and muscle either remained constant or increased at a slower rate --- this approach has been demonstrated clinically in [4]. Energy delivered in pulses takes advantage of the increased blood perfusion in skin and muscle relative to that in adipose tissue. Another approach could overlap treatment areas relative to the surface covered by the electrode; for example, displacing the electrode laterally 2/3 of its length would result in bordering response volumes, Fig. 6, and, consequently, uniform treatments.

In terms of device type, our study models the performance of a monopolar RF device, for which an active electrode delivers RF current at the treatment area and a much larger dispersive electrode (not explicitly shown in our simulation) returns the current to the device. Bipolar RF devices use two identical electrodes for delivery and return of RF current, thus, treatment takes place beneath both electrodes. The depth of bipolar RF treatment varies with the separation between electrodes. If they are next to each other, most of the RF will go through the skin. If they are adequately far apart then the treatment delivered by each electrode should be the same as the treatment delivered by a monopolar RF device. The duration of treatments that target adipose tissue vary from device to device but tend to be large, ranging from 45 min to 2 hours. The duration of the low-power RF exposure considered herein is about 2 hours. However at 45 min, temperature values are within 0.5 °C of its final value, see [5]. So the temperature profiles

do not change significantly between 45 min and 2 hours. However thermal damage is an accumulation process, thus, the response volume may be smaller at 45 min. In fact, the main clinical justification for large exposure durations is treatment response. The accumulation process of thermal damage is also a function of temperature, that is, at higher temperatures the accumulation of damage is faster. Hence, pulsed delivery of RF energy may also reduce the total exposure time.

]]

CONCLUSIONS

Safety and efficacy of treatment are central to any treatment and medical device. To this end, it is fundamental to understand and take into account effects and variations of morphology in RF-heating treatments of cutaneous and subcutaneous tissues. In the present work we have shown that the distribution of electric currents within subcutaneous tissues depends on tissue morphology, in particular, our results suggest that the distribution depends specifically on the density and orientation of the fibrous septa network. The electric field is more intense in septum oriented along the skin to muscle (top to bottom) direction, creating lines or planes of preferential heating. The more septum available for preferential heating, the larger the extent of volumetric RF-heating and thermal damage to the subcutaneous tissue. Thermal stresses alone, imposed by long-exposure heating up to approximately 50 ºC, result in small volumetric changes. Initially the septum expands with heating because it has a larger thermal and expansion coefficient, however, in the long-term the fat also expands occupying larger volumes and thinning the septum.

ACKNOWLEDGEMENTS

This work was supported by grant No. TEC2011-27133-C02-01 awarded by the Spanish "Plan Nacional de I+D+I del Ministerio de Ciencia e Innovación" to E. Berjano. A. González-Suárez was supported by VALi+d (ACIF/2011/194) and BFPI/2013/003 grants from the Generalitat Valenciana (Spain). Presentation of part of this work at the 2014 Annual Meeting of the American Society for Laser Medicine and Surgery was supported by a travel grant from the United States Air Force Office of Scientific Research to A. González-Suárez.

[[

APPENDIX

The model geometry domain was subdivided in 9 regions, see Figure A1. The mesh of the regions beneath the electrode was finer than adjacent regions. Beneath the electrode, the region corresponding to the adipose tissue had the finest mesh. The criterion used to subdivide the mesh was to make the simulation manageable for our computer workstation without losing spatial information --- the mesh is much finer where most of the heat transfer occurs. Mesh sizes were varied systematically until the magnitude of the maximum temperature changed less than 0.5% between simulations. Convergence test resulted in a grid size of 0.02 mm in the finest zone for both model geometries. The model meshes consisted of 30,545 and 45,208 elements for the intermediate and high spatial density fibrous septa architectures, respectively. In the model geometry of the intermediate-spatial density fibrous septa, the average thickness of septum is 0.418 ± 0.169 mm (n=72) and the maximum/minimum thicknesses are 1.052/0.105 mm. For the high-density fibrous septa model, the average thickness is 0.307 ± 0.121 mm (n= 99) and the maximum/minimum thicknesses are 0.628/0.126 mm. Clinical measurements of fibrous septa thickness obtained by MRI range from 0.277 to 2.18 mm [25].

The governing equations were solved simultaneously using the finite element method and a multi-frontal massively parallel sparse (MUMPS) direct solver in COMSOL Multiphysics 4.3b (COMSOL, Burlington, MA, USA). Simulations were run in a 64-bit PC with a 12-processor Intel Xeon platform running at 2.30 GHz with 8 GB of RAM. Time-dependent solutions were integrated to reach steady state, 8000 s with a time-step of 0.1 s. The thermo-elastic term couples the bioheat and motion equations, that is, the elastic response influences the thermal response and vice versa (two-way couple). The RF heating source one-way couples the electric equation to the other equations, that is, the electric response can be determined without knowledge of temperature or elastic deformation but the voltage distribution must be known to determine temperature and elastic responses. By considering equation terms, it seems like the electric equation could be solved first and the thermal and elastic equations next. However, for the electric and thermal equations the frame of reference is Eulerian and for the elastic deformation equation the frame of reference is Lagrangian. Therefore all equations are coupled in time because the location of RF heating sources could change as tissues underwent deformation.

]]

REFERENCES

1. Dierickx CC. The role of deep heating for noninvasive skin rejuvenation. Laser Surg Med 2006; 38(9):799–807.
2. Lolis MS, Goldberg DJ. Radiofrequency in cosmetic dermatology: A review. Dermatol Surg 2012; 38(11):1765–1776.
3. Sadick NS, Makino Y. Selective electro-thermolysis in aesthetic medicine: A review. Lasers Surg Med 2004; 34(2):91–97.
4. Franco W, Kothare A, Ronan SJ, Grekin RC, McCalmont TH. Hyperthermic injury to adipocyte cells by selective heating of subcutaneous fat with a novel radiofrequency device: Feasibility studies. Lasers Surg Med 2010, 42(5):361-370.
5. Jimenez Lozano JN, Vacas-Jacques P, Anderson RR, Franco W. Effect of fibrous septa in radiofrequency heating of cutaneous and subcutaneous tissues: computational study. Lasers Surg Med 2013, 45(5):326-38.
6. Mirrashed F, Sharp JC, Krause V, Morgan J, Tomanek B. Pilot study of dermal and subcutaneous fat structures by MRI in individuals who differ in gender, BMI, and cellulite grading. Skin Research and Technology 2004; 10(3):161-168.
7. Xu F, Lu T. Introduction to skin biothermomechanics and thermal pain. Berlin Heidelberg: Science Press Beijing and Springel-Verlag 2011.
8. Belenky I, Margulis A, Elman M, Bar-Yosef U, Paun SD. Exploring channeling optimized radiofrequency energy: a review of radiofrequency history and applications in esthetic fields. Advances in therapy 2012; 29(3):249-266.

9. Jiménez-Lozano J, Vacas-Jacques P, Anderson RR, Franco W 2012. Selective and localized radiofrequency heating of skin and fat by controlling surface distributions of the applied voltage: analytical study. Phys Med Biol; 57(22):7555-78.
10. Doss JD. Calculation of electric fields in conductive media. Med Phys 1982, 9(4):566-573.
11. Pennes HH. Analysis of tissue and arterial blood temperatures in the resting human forearm. J Appl Physiol 1948, 1(2):93-122.
12. Berjano EJ. Theoretical modeling of epicardial radiofrequency ablation: state-of-the-art and challenges for the future. Biomed Eng Online 2006; 5:24.
13. Franco W, Liu J, Romero-Méndez R, Jia W, Nelson JS, Aguilar G. Extent of lateral epidermal protection afforded by a cryogen spray against laser irradiation. Lasers Surg Med 2007; 39(5):414-421.
14. Pailler-Mattei C, Bec S, Zahouani H. In vivo measurements of the elastic mechanical properties of human skin by indentation tests. Med Eng Physics 2008; 30(5):599-606.
15. Comley K, Fleck NA. A micromechanical model for the Young's modulus of adipose tissue. Int J Solids Structures 2010; 47(21):2982-2990.
16. Deng Z-S, Liu J. Non-Fourier heat conduction effect on prediction of temperature transients and thermal stress in skin cryopreservation. J Thermal Stresses 2003; 26(8):7779-798.
17. Lin JC. Microwave Thermoelastic Tomography and Imaging. Advances in Electromagnetic Fields in Living Systems 2005; 4:41-76.
18. Miklavčič D, Pavšelj N, Hart FX. Electric properties of tissues. Wiley Encyclopedia of Biomedical Engineering 2006.
19. Haemmerich D, Schutt DJ, dos Santos I, Webster JG, Mahvi DM. Measurement of temperature-dependent specific heat of biological tissues. Physiol Meas 2005; 26(1): 59–67.

20. Bhattacharya A, Mahajan RL. Temperature dependence of thermal conductivity of biological tissues. Physiol Meas 2005; 24(3):769-783.
21. Henriques FC, Moritz AR. Studies of Thermal Injury: I. The Conduction of Heat to and through Skin and the Temperatures Attained Therein. A Theoretical and an Experimental Investigation. Am J Pathol 1947; 23(4):530-49.
22. Moritz AR, Henriques FC. Studies of Thermal Injury: II. The Relative Importance of Time and Surface Temperature in the Causation of Cutaneous Burns. Am J Pathol 1947; 23(5):695-720.
23. Weaver JA, Stoll AM. Mathematical model of skin exposed to thermal radiation. Aerospace Med 1969; 40(1):4–30.
24. Arnoczky SP, Aksan A. Thermal modification of connective tissues: basic science considerations and clinical implications. The Journal of the American Academy of Orthopaedic Surgeons 2000; 8(5):305-313.
25. Hexsel DM, Abreu M, Rodrigues TC, Soirefmann M, do Prado DZ, Gamboa MM. Side-by-side comparison of areas with and without cellulite depressions using magnetic resonance imaging. Dermatol Surg. 2009 Oct; 35(10):1471-7.

Table 1. Mechanical, thermal, electrical and physiological properties of the skin, fat, fibrous septa and muscle [4, 14-17]: ε_r, relative permitivity (vacuum permitivity, $\varepsilon_0 = 8.854\times10^{-12}$ F/m); κ, electric conductivity; k, thermal conductivity; ρ, density; c, specific heat; ω, blood perfusion rate; E, Young's Modulus; and α, thermal expansion coefficient.

Element	ε_r	κ **(S/m)**	k **(W/m·K)**	ρ **(kg/m^3)**	c **(J/kg·K)**	ω **(kg/m^3·s)**	E **(kPa)**	α **(1/°C)**
Skin	1832.8	0.22	0.53	1200	3800	2	35	6×10^{-5}
Fat	27.22	0.025	0.16	850	2300	0.6	2	2.76×10^{-5}
Muscle	1836.4	0.5	0.53	1270	3800	0.5	80	4.14×10^{-5}
Septa	1832.8*	0.22*	0.53*	1200*	3800*	0**	0.09	6×10^{-5}*

* Assumption. ** The perfusion term in the septa is neglected (i.e. fibrous septa as solid).

Table 2. Electrical, thermal and elastic boundary conditions: L, RF applicator half-length; l_s, $l_{f,c}$ and l_m, skin, subcutaneous tissue and muscle layer thicknesses, respectively; W, domain half-width; T_a, ambient temperature; T_c, constant core body temperature; T_r, electrode temperature; $h_{a\text{-}s}$, air-skin heat transfer coefficient; $\boldsymbol{J}$, current density vector.

Location	**Electric**	**Thermal**	**Elastic**
$y = 0$	$\{n\cdot\boldsymbol{J}=0 \mid -W<x<-L\}$, $\{V=V_0 \mid -L<x<L\}$, $\{n\cdot\boldsymbol{J}=0 \mid L<x<W\}$	$\{\boldsymbol{n}\cdot k\nabla T=h_{a-s}(T_a-T) \mid -W<x<-L\}$, $\{T=T_r \mid -L<x<L\}$, $\{\boldsymbol{n}\cdot k\nabla T=h_{a-s}(T_a-T) \mid L<x<W\}$	$\{\boldsymbol{u}=0 \mid -W<x<W\}$
$y = -(l_s+l_{f,c}+l_m)$	$\{V=0 \mid -W<x<W\}$	$\{T=T_c \mid -W<x<W\}$	$\{\boldsymbol{u}=0 \mid -W<x<W\}$
$x = -W$	$\{n\cdot\boldsymbol{J}=0 \mid -(l_s+l_{f,c}+l_m)<y<0\}$	$\{n\cdot k\nabla T=0 \mid -(l_s+l_{f,c}+l_m)<y<0\}$	$\{\boldsymbol{u}=free \mid -(l_s+l_{f,c}+l_m)<y<0\}$
$x = W$	$\{n\cdot\boldsymbol{J}=0 \mid -(l_s+l_{f,c}+l_m)<y<0\}$	$\{n\cdot k\nabla T=0 \mid -(l_s+l_{f,c}+l_m)<y<0\}$	$\{\boldsymbol{u}=free \mid -(l_s+l_{f,c}+l_m)<y<0\}$

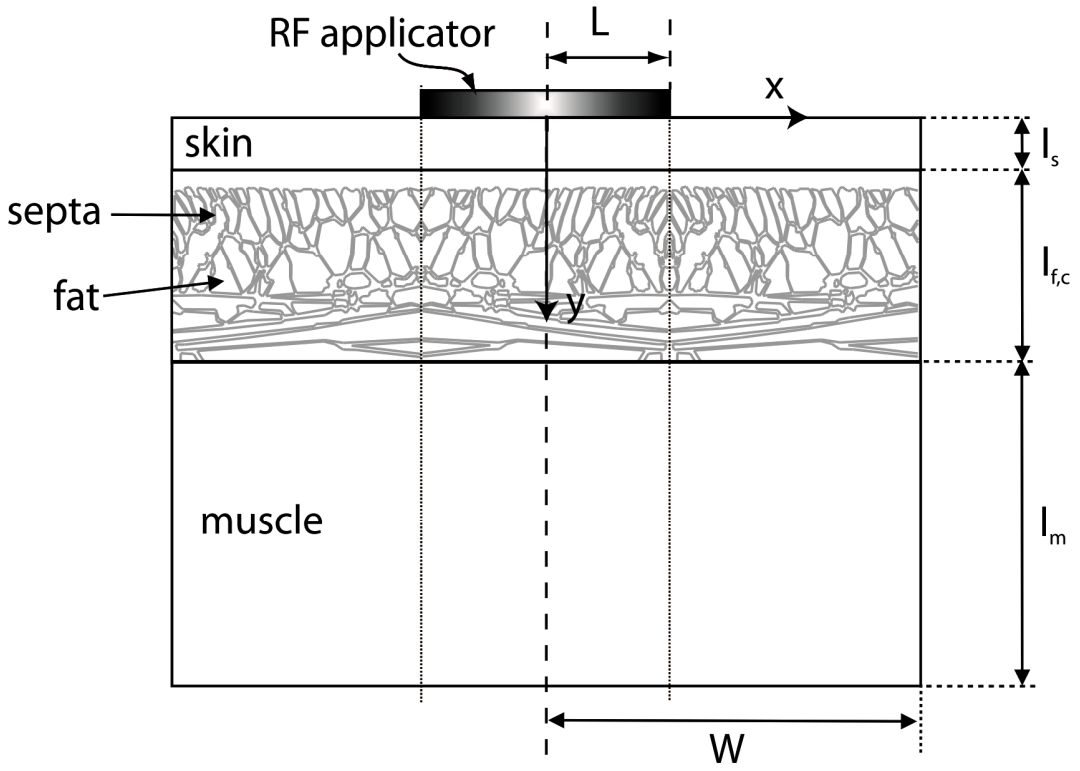

Figure 1. Model geometry of a high-density network of fibrous septa with an RF applicator (active electrode) atop skin, subcutaneous tissue --- constituted by fibrous septa and fat --- and muscle. Thicknesses of skin, l_s, subcutaneous tissue, $l_{f,c}$, and muscle, l_m, layers are respectively 1.5, 17, and 38 mm. W = 54.5 mm. L =18.5 mm. The RF applicator is actively cooled to maintain the temperature of the skin surface at 30 ºC. $-W < x < W$ and $-(l_s+l_{f,c}+l_m) < y < 0$ define the numerical domain. Vertical dotted lines indicate the mirror planes used to extend the lateral domain in order to eliminate numerical artifacts.

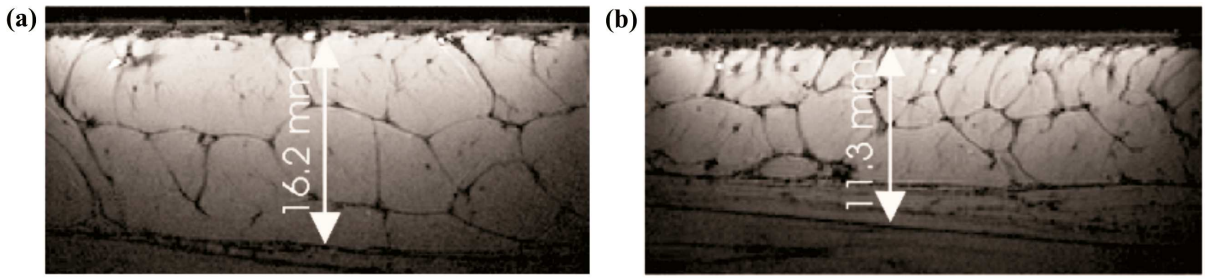

Figure 2. High-resolution in vivo MRIs of subcutaneous adipose tissue [6], dark filaments correspond to fibrous septa within the subcutaneous tissue: (a) Cellulite Grade 2.5, intermediate-density of fibrous septa, (b) Cellulite Grade 0, smooth skin, high-density of fibrous septa.

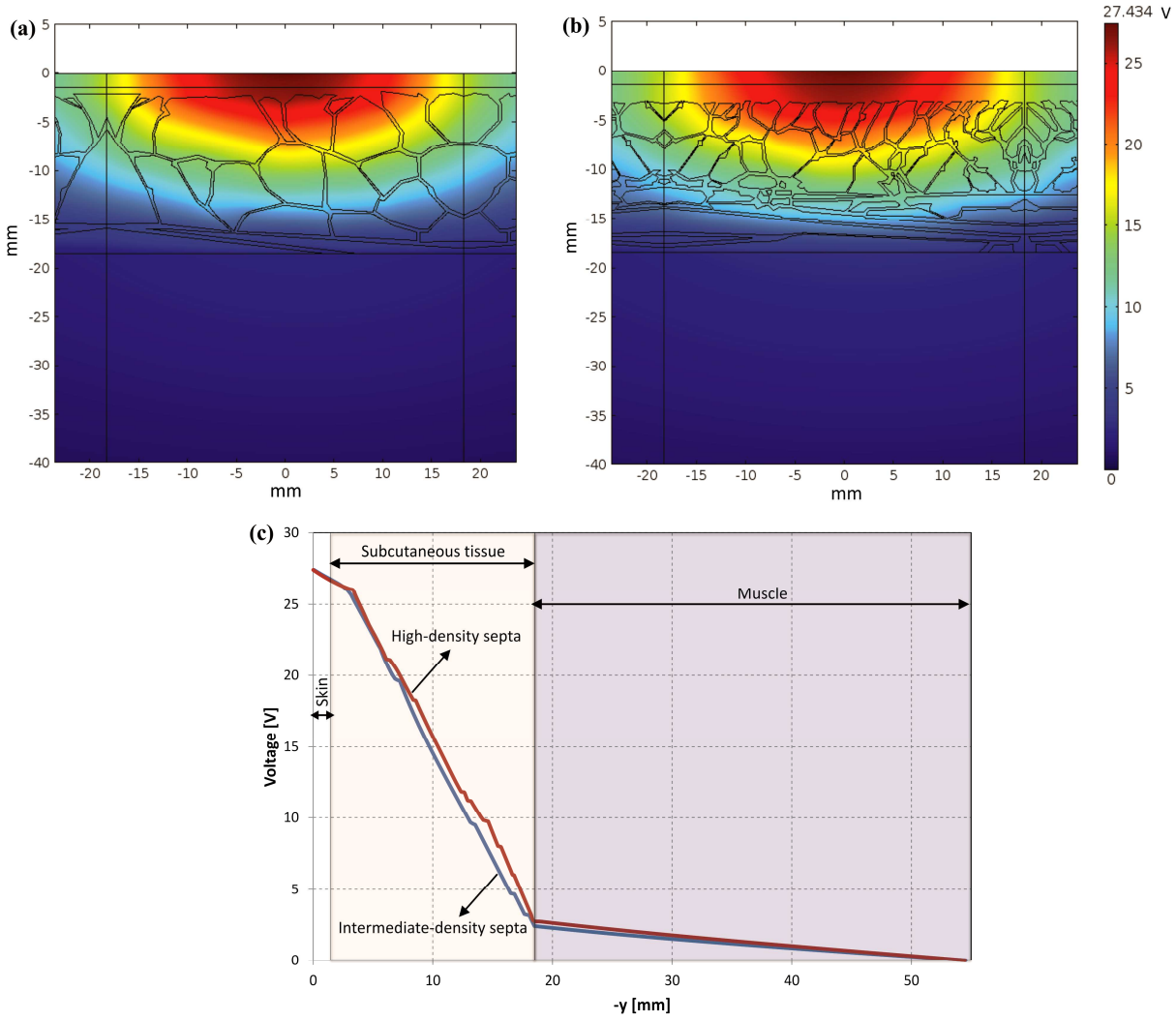

Figure 3. Voltage distributions for (a) intermediate- and (b) high-density fibrous septa architectures at the same color bar scale. (c) Voltage depth profiles at $x = 0$ for both architectures.

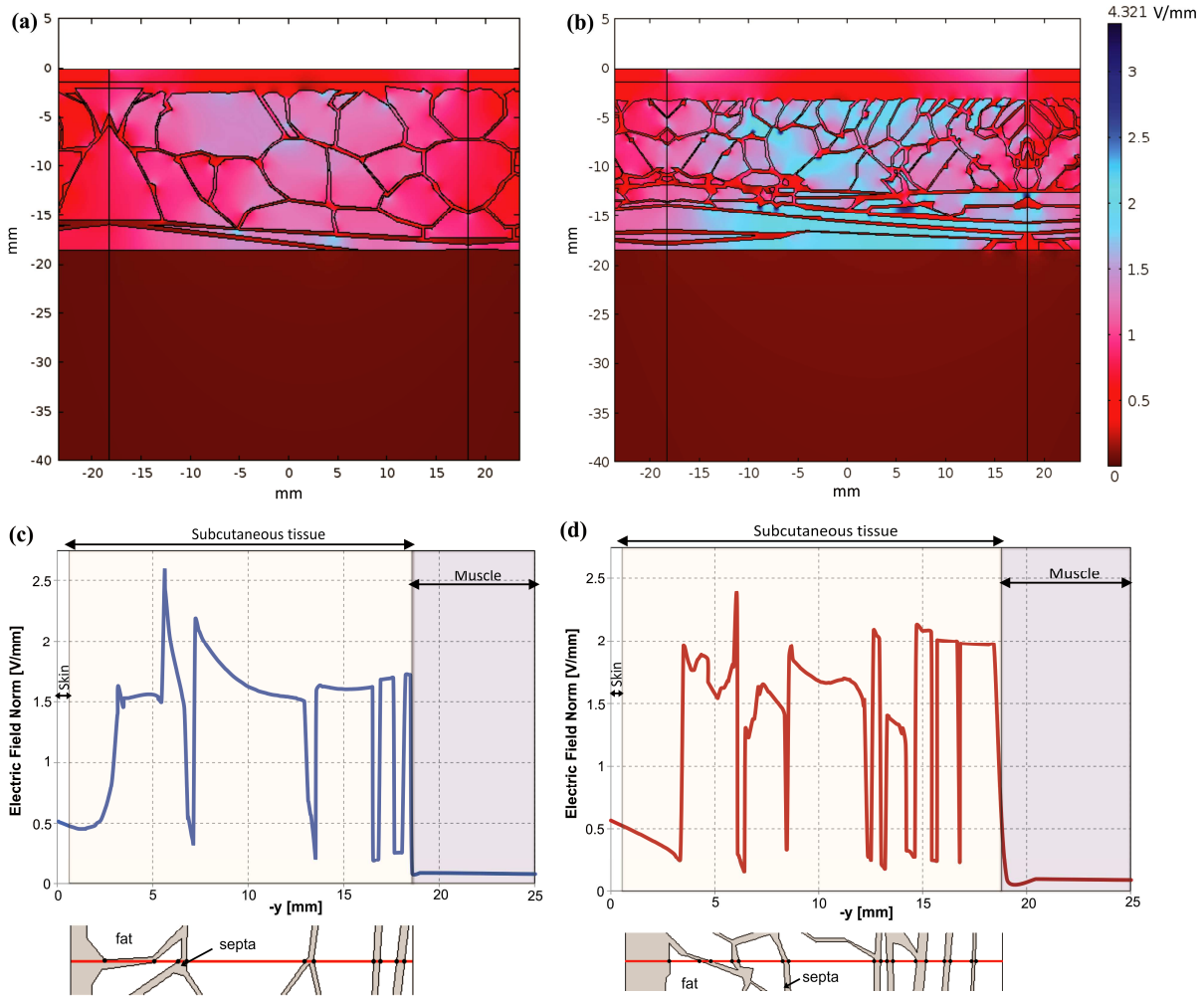

Figure 4. Electric field norm distributions for (a) intermediate- and (b) high-density fibrous septa architectures at the same color bar scale. Electric field depth profiles at $x = 0$ for (c) intermediate and (d) high-density fibrous septa architectures, bottom inserts show the tissue paths along $x = 0$.

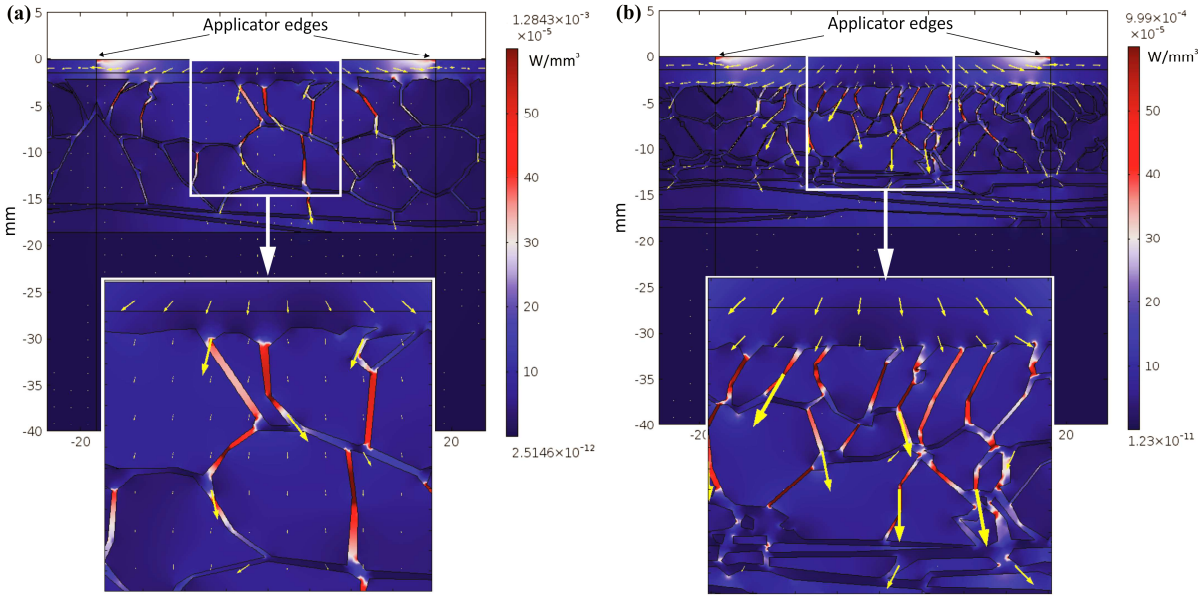

Figure 5. Distributions of power absorption and electric displacement field (arrows) for (a) intermediate- and (b) high-density fibrous septa architectures.

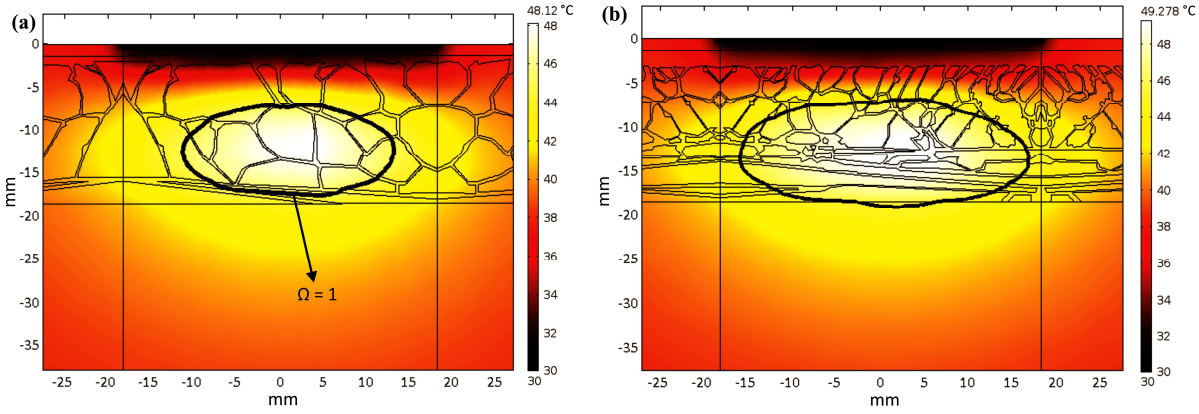

Figure 6. Temperature distributions at steady state (t = 8000 s) for (a) intermediate and (b) high-density fibrous septa architectures. Solid line contours denote the extent of irreversible thermal damage, Ω =1.

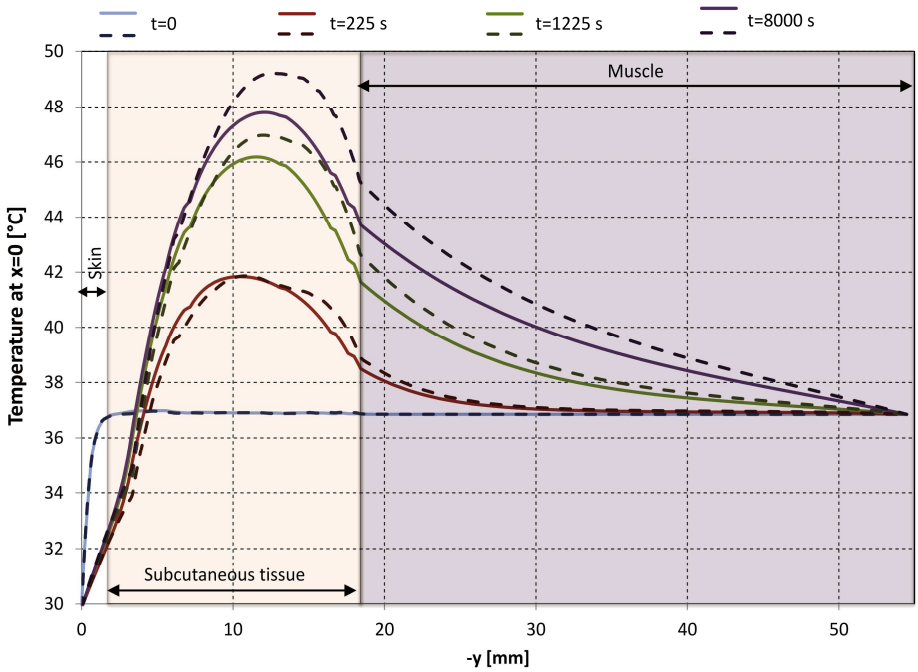

Figure 7. Time evolution of temperature depth profiles at $x = 0$ for intermediate (solid lines) and high-density (dashed lines) fibrous septa architectures.

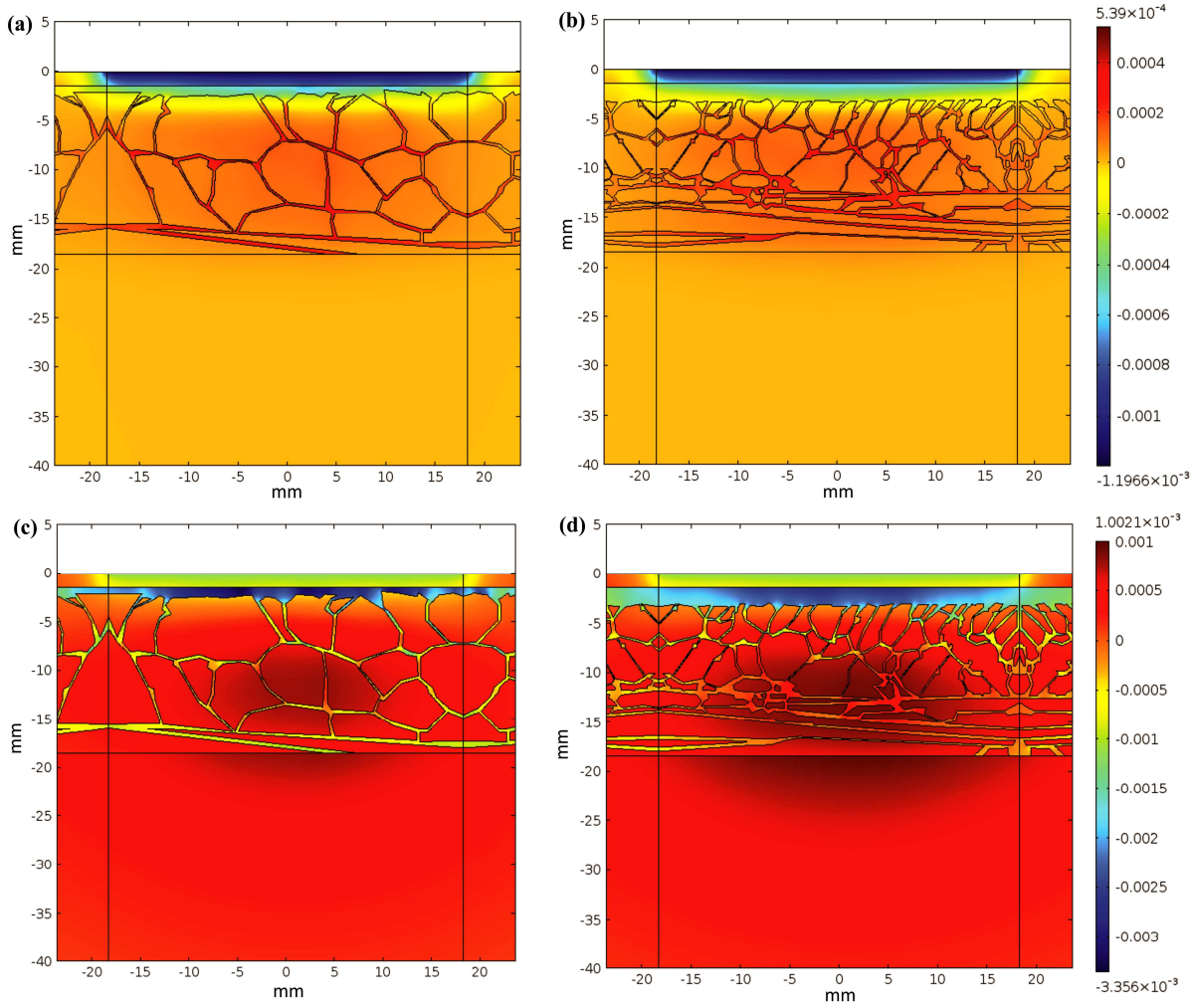

Figure 8. Volumetric strain distributions, intermediate-density fibrous septa architecture at (a) t=25 and (c) 8000 s and high-density fibrous septa architecture at (b) t=25 and (d) 8000 s. Color bar scale on top and bottom are valid for distributions at t=25 and 8000 s, respectively.

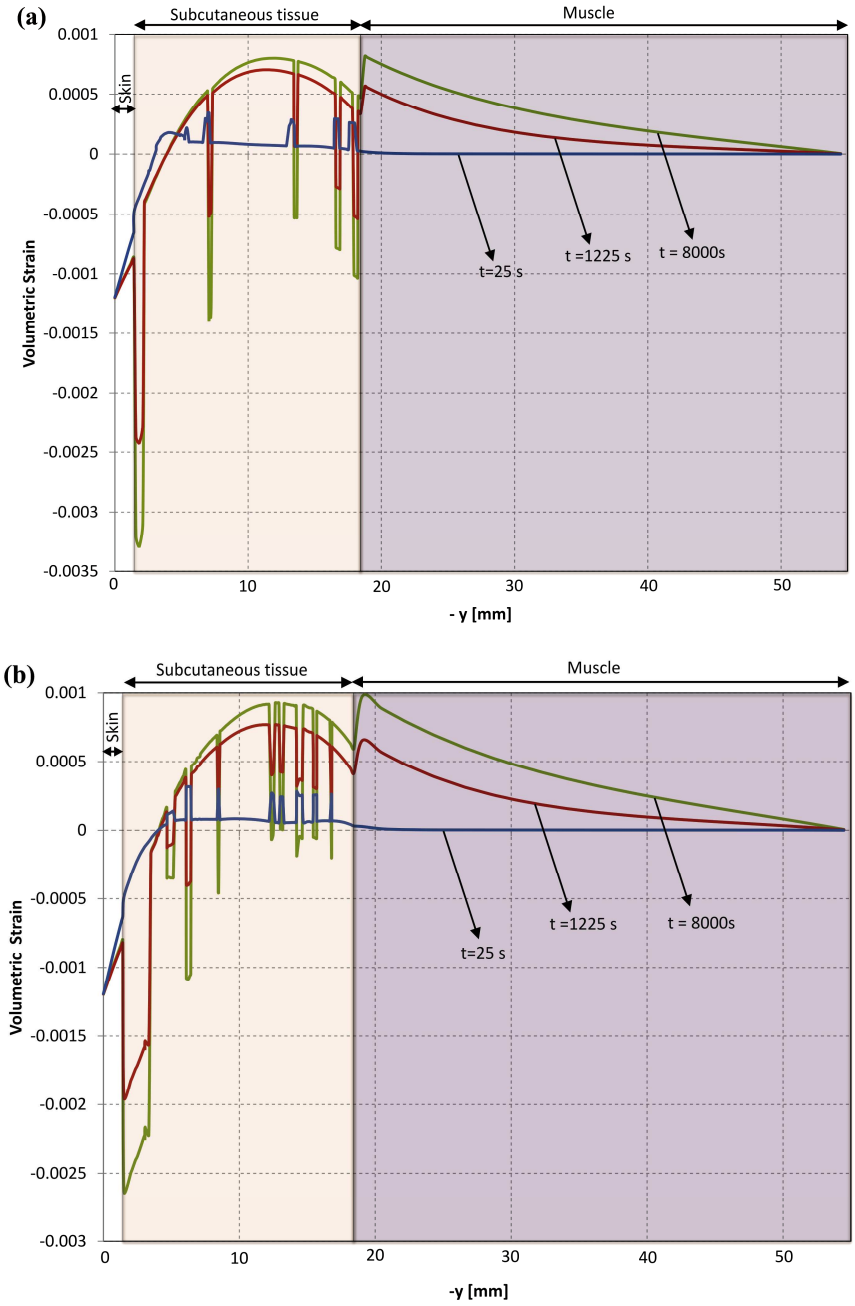

Figure 9. Time evolution of volumetric strain depth profiles at $x = 0$ for (a) intermediate- and (b) high-density fibrous septa architectures.

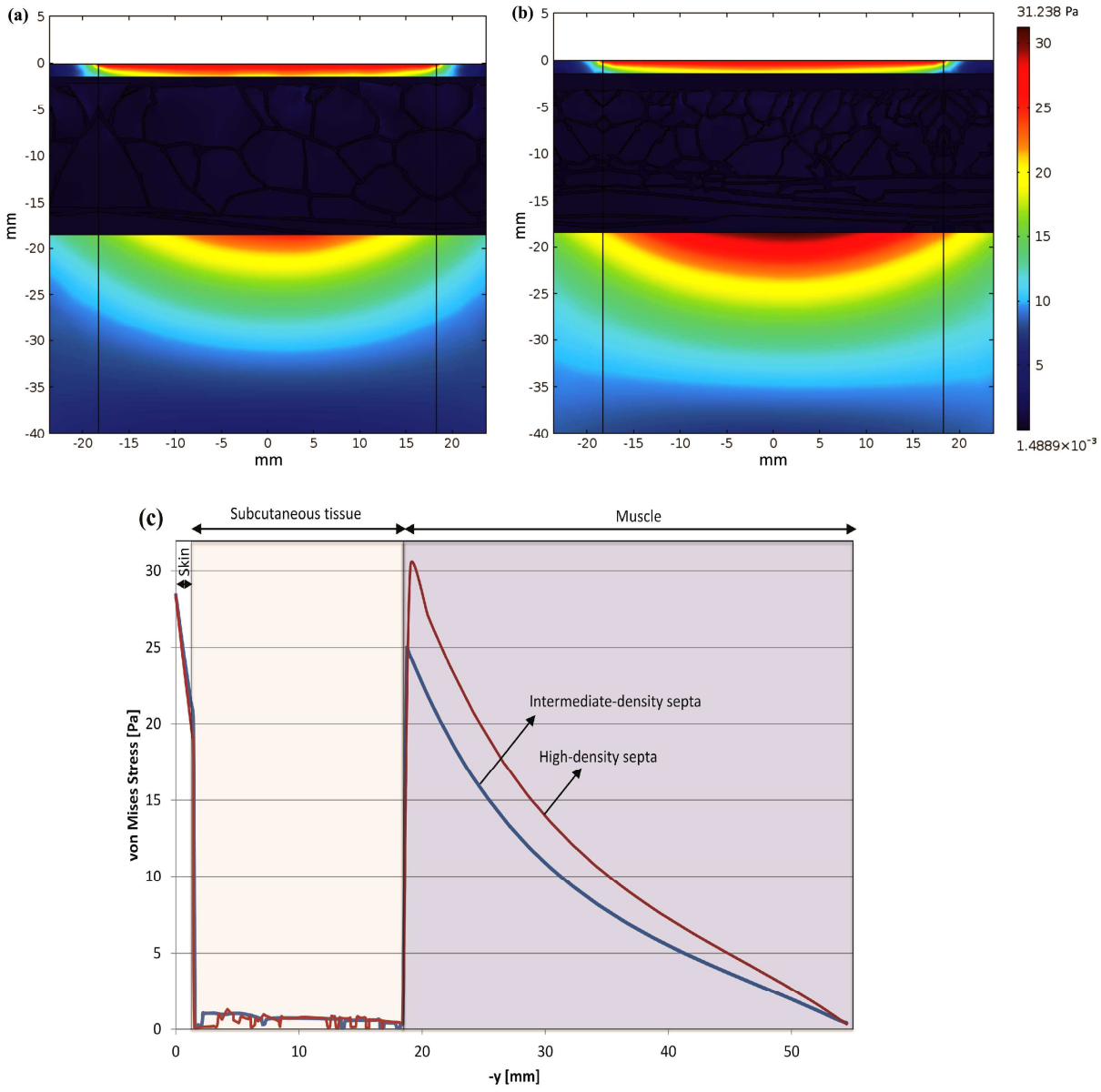

Figure 10. Von Mises stress distributions for (a) intermediate- and (b) high-density fibrous septa architectures. (c) Von Mises stress depth profile at $x = 0$ for both architectures.

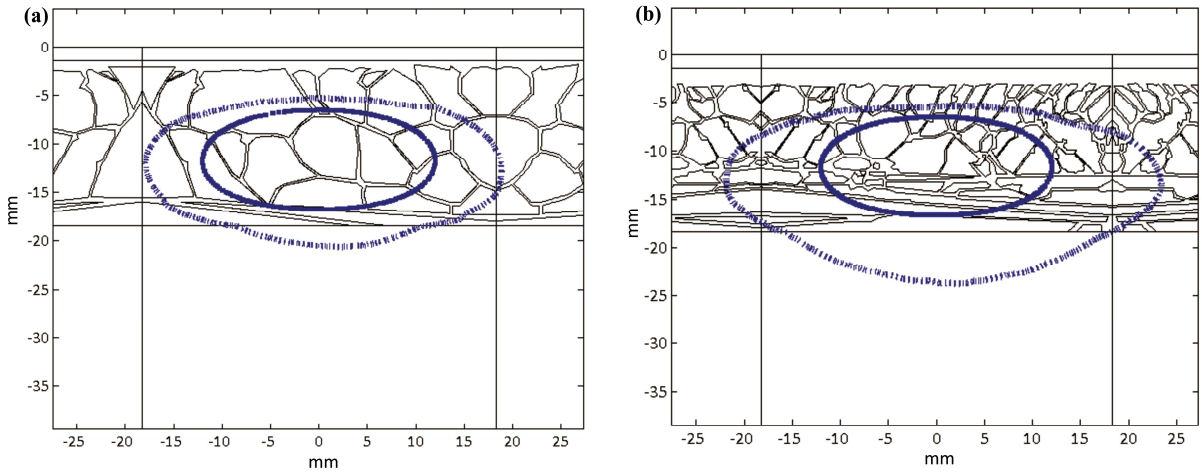

Figure 11. Thermal damage response to long RF-heating exposures, t = 8000 s for (a) intermediate- and (b) high-density fibrous septa architectures. Contours correspond to 63% loss in cell viability (Ω =1). Solid line contours represent damage to a homogenous fat layer that neglects the fibrous septa. Dashed line contours represent damage to a tissue layer constituted by fibrous septa and fat.

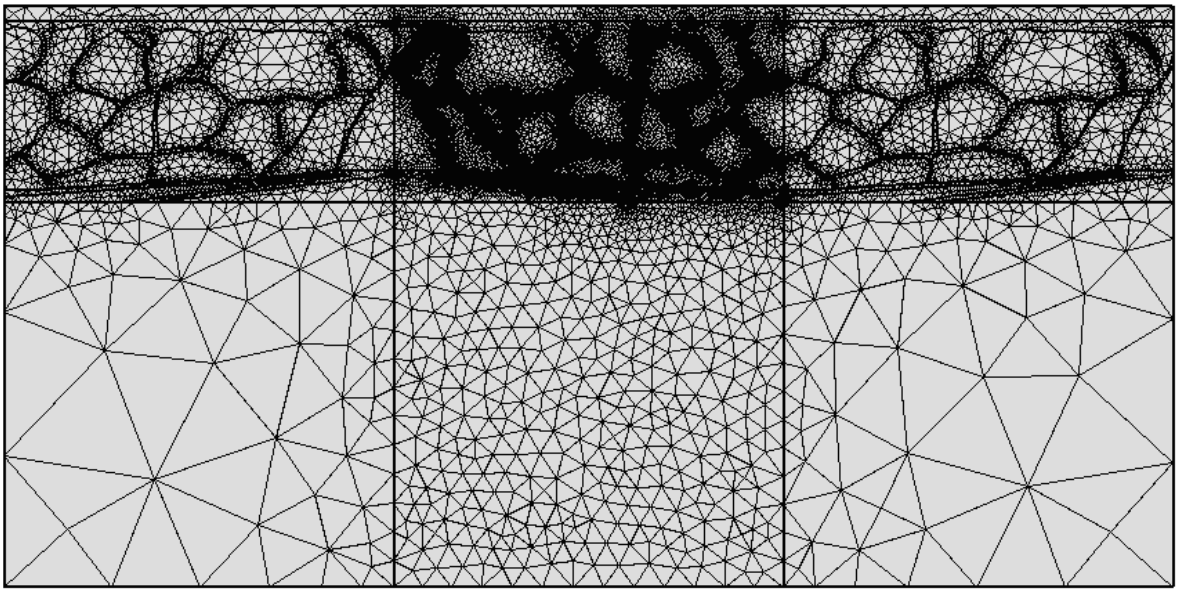

Figure A1. Model geometry mesh of intermediate spatial density fibrous septa architecture.